Materials Advances

ROYAL SOCIETY OF CHEMISTRY

PAPER

View Article Online
View Journal | View Issue

Cite this: *Mater. Adv.*, 2026, 7, 1884

Numerical investigation of high-performance bilayer tin-based perovskite solar cells with SCAPS-1D

Hariharan Rajasekaran, Thangaraji Vasudevan and Lung-Chien Chen *

A comprehensive simulation-based investigation was conducted on an advanced, lead-free perovskite solar cell (PSC) design. This cell achieved high performance through its novel absorber architecture, which utilized a dual-layer configuration made of tin-based perovskite materials ($CsSnI_3$ and $CsSnCl_3$). Simulations were carried out to determine device performance and stability limits by employing the SCAPS-1D software tool. The device structure was designed to enable bandgap alignment with $CsSnI_3$, which was used as a narrow bandgap material to act as a light harvester, and $CsSnCl_3$, which was used as a wider bandgap material to act as a charge and defect passivation layer. Prior to the simulations, necessary material parameter details, such as the orbital components forming the band edges and bandgap widening, were thoroughly verified. RIGOROUS simulations on SCAPS-1D revealed a maximum power conversion efficiency (PCE) value of 30.02% (FF = 88.56%, J_{sc} = 32.09 mA cm^{-2}, and V_{oc} = 1.05 V) when optimal parameter inputs were used. Important stability constraints on various PSC devices were obtained by precisely modelling the defects, which resulted in PCE failure when either the interface defect density value and/or the respective bulk density value of either $CsSnI_3$/$CsSnCl_3$ layer exceeded 1×10^{15} cm^{-3}. Therefore, high-quality materials are mandatory. In addition, thermal stability analysis indicated that the PCE value is inversely related to temperature. Importantly, the analysis indicates that the voltage component V_{oc} influences the PCE value predominantly.

Received 10th December 2025,
Accepted 1st January 2026

DOI: 10.1039/d5ma01437a

rsc.li/materials-advances

1. Introduction

Perovskite solar cells (PSCs) have attracted considerable attention owing to their high power conversion efficiency (PCE), which reaches 26%, and their very low-cost fabrication process.[1–3] Moreover, their tunable bandgap, long carrier diffusion ranges, and solution processability render them promising for future solar cells. Recently, nanocrystals of all-inorganic caesium lead halide perovskites (PVSKs) ($CsPbY_3$, wherein Y is a halogen atom) have been synthesized, and they exhibit exceptional optoelectronic attributes as well as easy solution-processing.[4,5] Although their brilliant performance has attracted great attention, their toxicity due to the presence of environmentally hazardous lead is a very important concern that is yet to be properly alleviated.[6] To alleviate such toxicity, recent attempts have been directed towards exploring alternatives, more environmentally friendly materials, and tin-containing PVSKs ($CsSnY_3$) have recently emerged as very promising materials.[7–9] Although tin- and lead-containing PVSKs possess remarkable optoelectronic attributes owing to their identical electronic configuration, their toxicity is yet to be properly alleviated. In tin-containing PVSKs, the high instabilities of Sn^{2+} towards oxidation to Sn^{4+} under ambient conditions (which cause the formation of p-type self-doped materials) and the high recombination rate of charge carriers significantly impede device stability and efficiency.[10–12] Although $CsSnY_3$ PVSKs offer great benefits owing to their optimal bandgap, high carrier mobility, and less adverse effects on the environment compared with those of their counterpart Cd- and Pb-based materials,[13] their further utilization is impeded by their instabilities.

Among Sn-based halide PVSKs, $CsSnI_3$ has become a reassuring light-harvesting material because of its direct bandgap ($\sim$1.3 eV), strong optical absorption in the visible to near-infrared regions, and robust defect-independent electronic band structure.[14,15] $CsSnI_3$ exhibits low stability under atmosphere ambient, which restricts its applications involving long lifetimes. However, a promising route to optimizing efficiency and robustness simultaneously involves the design of bilayer and graded bandgap absorber designs by incorporating $CsSnI_3$ and wide-bandgap PVSKs, such as $CsSnCl_3$.[16] As $CsSnCl_3$ has a wider bandgap of $\sim$2.3 eV, it acts satisfactorily as a 'window'

Department of Electro-Optical Engineering, National Taipei University of Technology, Taipei City 10608, Taiwan, Republic of China.
E-mail: rhariharan318@gmail.com, orgthangaraji@gmail.com, ocean@ntut.edu.tw; Tel: (+886)-2-2771-2171

layer, increasing the band match and blocking recombination at interfaces.[17] The $CsSnCl_3$/$CsSnI_3$ bilayer structure has several beneficial attributes: (i) dual-band optical absorption because of the wide and narrow bandgap materials, which augment light and carrier concentration simultaneously;[18] (ii) the graded band profile enables efficient carrier separation and hinders recombination, and (iii) $CsSnCl_3$ acts as an oxidation passivation agent and protects $CsSnI_3$ layers against oxidation, which degrades device stability.[19] This design takes inspiration from band engineering methods adopted by high-efficiency Pb-based tandems and PSCs but is applicable to a completely lead-free structure.

Further optimization of device performance requires the selection of appropriate charge transport layers. PCBM (phenyl-C_{61}-butyric acid methyl ester) is commonly employed as an ETL because of its high electron mobility, good energy-level alignment with the conduction bands of PVSKs, and ability to reduce interfacial recombination.[20,21] On the other hand, Cu_2SnS_3 (CFTS) has recently attracted attention as a suitable HTL material because of its earth-abundant components, chemical stability, proper work function, and compatibility with the absorbers of PVSKs.[22–24] The employment of CFTS as a nontoxic and stable HTL opens up a more environmentally friendly pathway over conventional organic HTL materials, such as Spiro-OMeTAD, which are restricted because of their high cost and poor long-term stability.[25] As a result, the device architecture PCBM/$CsSnCl_3$/$CsSnI_3$/CFTS represents a totally lead-free inorganic PSC that has optimized interfaces for efficient charge transport coupled with enhanced stability during device operation. This device architecture not only minimizes the toxicity issues but also inherits the synergistic advantages of bilayer absorbers, inorganic stability, and environmentally benign transport layers.[26,27] Recent simulations and experimental investigations have pointed out that the critical optimization of the thickness of bilayer absorbers is highly necessary to balance the competing processes of light absorption and charge transport, which directly influence the V_{oc}, J_{sc}, and FF.[28–30,39,40]

This research focuses on a fully lead-free solar cell structure (PCBM/$CsSnCl_3$/$CsSnI_3$/CFTS) and uses one-dimensional semiconductor simulation (SCAPS-1D) to explore the impact of the thickness of the absorber layer on the overall device efficiency and operation. Although most studies have focused on either single-absorber $CsSnY_3$-based devices or Pb-based bilayer architectures, our effort exceptionally probes the synergistic $CsSnCl_3$/$CsSnI_3$ bilayer as well as the ecologically friendly charge transport layers. We report critical insights into the rational design of stable and highly efficient lead-free PSCs through thickness-dependent changes in the PCE, J_{sc}, FF, and V_{oc}. The findings underscore that the strategic engineering of the bilayer, in concert with ecologically friendly transport materials, can offer a realistic pathway toward next-generation, sustainable photovoltaic devices.

2. Methodology and modelling

2.1. Density functional theory calculations

Density functional theory (DFT) calculations were used to examine the electronic characteristics of $CsSnI_3$ and $CsSnCl_3$ with the Quantum ESPRESSO package (v7.4.1).[31] The Perdew–Burke–Ernzerhof (PBE) functional was employed, which is a type of generalized gradient approximation (GGA), to effectively model the exchange and correlation effects governing electron–electron interactions. Scalar-relativistic standard-preserving pseudopotentials were utilized for Cs, Sn, I, and Cl. To achieve sufficient precision and ensure the convergence of the total energy, the simulation employed a plane-wave cutoff energy set at 60 Rydberg (Ry). Additionally, the Brillouin zone was sampled using a $6 \times 6 \times 6$ Monkhorst–Pack mesh, which successfully limited the residual error in the total energy calculation to less than 10^{-6} Ry. The cubic crystal structures of $CsSnI_3$ and $CsSnCl_3$ were fully optimized such that the forces affecting every atom were less than 10^{-3} Ry $Bohr^{-1}$. Subsequently, the density of states and electronic band structures were computed based on the relaxed geometries, with vacuum-level alignment applied to reference energy levels relative to the Fermi energy. All the simulations were performed utilizing Quantum ESPRESSO, a publicly available plane-wave DFT software package.[31]

2.2. Governing laws and equations in SCAPS-1D modeling

SCAPS-1D, a simulator application that was first designed and developed at Ghent University under the guidance of Professor M. Burgelman, has been extensively employed for modelling diverse solar cell architectures.[32] In this research, we conducted numerical simulations using SCAPS-1D (version 3.3.12). The software allows the incorporation of up to seven layers, along with front and back contacts, as input parameters. Key device metrics, such as the PCE (η), J_{sc}, FF, current–voltage (J–V), and spectral response (QE) characteristics, can be evaluated. The simulations are principally controlled by the interaction of two fundamental physical laws: the distribution of the internal electric field is explained by Poisson's eqn (1), while the transport and conservation of electrons and holes are described by the continuity eqn (2).

$$\frac{d^2\psi}{dx^2} = \frac{e}{\varepsilon_0\varepsilon_r}[l(x) - m(x) + N_D - N_A + \rho_l - \rho_m], \quad (1)$$

where ψ is the electrostatic potential; l and m are the electron and hole concentrations, respectively; ε_0 is the vacuum; and ε_r is the relative permittivity. N_D and N_A are the donor and acceptor doping densities, respectively, and ρ_m and ρ_l are the electron and hole distributions, respectively.

$$\frac{dJ_l}{dx} = \frac{dJ_m}{dx} = O - P, \quad (2)$$

where P represents the recombination rate, O denotes the generation rate, and J_m and J_l are the electron and hole densities, respectively.

The drift and diffusion equations are given by eqn (3) and (4), respectively:

$$J_n = D_m\frac{dm}{dx} + \mu_m m\frac{d\varphi}{dx}, \quad (3)$$

$$J_p = D_l\frac{dl}{dx} + \mu_m l\frac{d\varphi}{dx}, \quad (4)$$

Table 1 The set of material values used to simulate $CsSnI_3$, $CsSnCl_3$, and charge transport layer performance in SCAPS-1D[23,26,37,38]

Parameter	FTO	PCBM	$CsSnI_3$	$CsSnCl_3$	CFTS
Thickness (μm)	0.5	0.05	0.1–1.5	0.15 (varied)	0.1
E_g (eV)	3.5	2	1.3	1.52	1.3
X (eV)	4	3.9	3.6	3.90	3.3
ε_r	9	3.9	9.93	29.4	9
N_c (cm^{-3})	2.2×10^{18}	2.5×10^{21}	1×10^{19}	1×10^{19}	2.2×10^{18}
N_v (cm^{-3})	1.8×10^{19}	2.5×10^{21}	1×10^{18}	1×10^{19}	1.819
μ_n ($cm^2\ V^{-1}\ s^{-1}$)	20	0.2	1.5×10^3	2	21.98
μ_h ($cm^2\ V^{-1}\ s^{-1}$)	10	0.2	5.85×10^2	2	21.98
N_A (cm^{-3})	0	0	10^{21}	1×10^{15}	1×10^{18}
N_D (cm^{-3})	1×10^{21}	2.93×10^{17}	0	0	0
N_t (cm^{-3})	1×10^{15}	1×10^{15}	1×10^{13}	1×10^{13}	1×10^{15}

where the diffusion coefficient of the electrons is denoted as D_m and the electron, hole mobility is denoted as μ_x.

To complement the atomic-scale insights obtained from DFT, the solar energy efficiency of the $CsSnI_3/CsSnCl_3$ bilayer solar cell was investigated through device-level simulations using SCAPS-1D (solar cell capacitance simulator). SCAPS-1D is a one-dimensional modeling application widely utilized for thin-film photovoltaic cells. This structure facilitates the in-depth examination of the electrical, optical, and recombination processes within multilayer device structures. The bilayer absorber was constructed by stacking $CsSnI_3$ and $CsSnCl_3$ with thicknesses optimized according to material parameters derived from DFT calculations and previous reports. Key inputs included bandgap energies, electron affinities, dielectric constants, effective density of states, carrier mobilities, and defect densities. Attention was devoted toward interface defect density and band alignment, extracted from DFT electrostatic potential analysis, to realistically capture charge transport and recombination dynamics at the heterojunction.

To maintain model integrity, the numerical input parameters for the SCAPS-1D simulation, specifically the dielectric constants, carrier effective masses, and mobilities, were sourced from established theoretical literature and experimental details (as detailed in Table 1) rather than directly from the DFT calculations. While DFT was employed in this study to offer a qualitative understanding of the electronic structure and orbital hybridization of the bilayer interface, the SCAPS-1D framework utilizes literature-validated values to maintain consistency with recognized benchmarks. Furthermore, the adoption of a 1.52-eV bandgap for the $CsSnCl_3$ layer, rather than its bulk value of ~3.0 eV, is a strategic choice representing an optimized Cl-rich mixed-halide interface layer ($SnI_{3-x}Cl_x$). This value is consistent with high-performance Sn-halide heterojunction simulations[23,26,37,39,40] and ensures the ideal graded band alignment required to maximize charge extraction while suppressing interfacial recombination.

The parameters for the material and interface used in the simulations are summarized in Tables 1 and 2. FTO was treated as a wide-bandgap degenerate semiconductor with high donor concentration to ensure transparency and conductivity, while PCBM was assigned a 2.0-eV bandgap with low carrier mobilities, consistent with its role as the ETL. The $CsSnI_3$ absorber was modelled with a tunable thickness (0.1–1.5 μm), a 1.3-eV direct bandgap, and high carrier mobilities. Conversely, $CsSnCl_3$ was represented with a fixed thickness of 150 nm (varied in bilayer configurations), a slightly larger bandgap of 1.52 eV, a high dielectric constant (ε_r = 29.4), and comparatively lower mobilities, reflecting its transport limitations.

CFTS, employed as the hole transport material, was defined with balanced carrier mobilities (~22 $cm^2\ V^{-1}\ s^{-1}$) and a moderate electron affinity (3.3 eV), ensuring efficient hole extraction. To account for recombination effects, defect densities were set to 10^{13} cm^{-3} for the bulk layers, and neutral interfacial trap states with a capture cross-section of 10^{-19} cm^2 and 10^{10} cm^{-2} for density were introduced at the CFTS/$CsSnI_3$, $CsSnI_3/CsSnCl_3$, and $CsSnCl_3$/PCBM interfaces. These carefully chosen parameters enabled the simulations to reproduce trends consistent with those in the existing literature and reveal the performance improvements achieved in this work.

Illumination was modelled under typical AM1.5G solar spectrum conditions. The solution process involved solving Poisson's equation and the continuity equations (for both electrons and holes) concurrently and iteratively (self-consistently) throughout the entire simulated device structure. From the simulated J–V

Table 2 Interface defect parameters considered in SCAPS-1D simulations. For each interface (CFTS/$CsSnI_3$, $CsSnI_3/CsSnCl_3$, and $CsSnCl_3$/PCBM), capture cross-sections, energetic distribution, the total defect density, reference energy level, and defect type are summarized. Neutral defect states located above the valence band maximum were assumed in the modelling

Interface	Defect charge state	Electron/hole capture cross section (cm^2)	Energetic distribution	Defect energy level reference	Integrated defect density (cm^{-2})
CFTS/$CsSnI_3$	Neutral	1×10^{-19}	[a]	[b]	1×10^{-10}
$CsSnI_3/CsSnCl_3$	Neutral	1×10^{-19}	[a]	[b]	1×10^{-10}
$CsSnCl_3$/PCBM	Neutral	1×10^{-19}	[a]	[b]	1×10^{-10}

[a] Single. [b] Above the VB maximum.

characteristics, key solar cell measurements like the FF, PCE, V_{oc}, and J_{sc} were determined. A thickness-dependent study was performed by altering the depth of the active material layer from 0.3 to 1.5 μm to assess its influence on light absorption, carrier collection, and recombination processes. The results confirmed the DFT-based hypothesis that the graded bandgap bilayer facilitates efficient charge separation while suppressing recombination losses, resulting in the best possible device performance at a 1.5-μm absorber thickness.

A sensitivity analysis was conducted regarding the assumptions of the interface layer properties. The performance of the device was notably affected by the alignment of the bandgap at the $CsSnI_3/CsSnCl_3$ heterojunction. An increase in the interface bandgap beyond 1.55 eV causes a drop in the J_{sc} due to increased extraction barriers; reducing it below 1.50 eV led to higher interfacial recombination. This confirms that the selection of 1.52 eV representing an optimized mixed-halide interface is the critical 'sweet spot' for achieving the peak efficiency of 30.02%.

The combination of DFT and SCAPS-1D enables a deep understanding of how the material properties interact with device architecture to provide proper guidance for the rational design of efficient and lead-free PSCs.

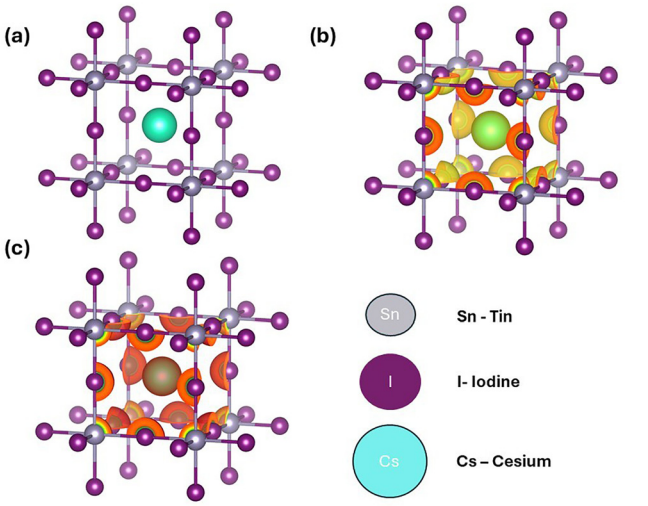

Fig. 1 (a) Crystal structure of the $CsSnI_3$ perovskite, where Cs atoms occupy the cub-octahedral cavities and Sn is octahedrally coordinated by I atoms. (b) Charge density distribution illustrating strong localization around I atoms with hybridization among the Sn-5s and I-5p orbitals, indicative of mixed ionic-covalent bonding. (c) Electrostatic potential profile revealing potential wells at I sites and a relatively smooth potential landscape, which promotes effective charge movement and reduces carrier recombination.

3. Results and discussion

3.1. Charge density and electrostatic potential analysis of $CsSnI_3$ and $CsSnCl_3$

In Fig. 1(a), the crystal structure of $CsSnI_3$ is depicted, where Cs atoms occupy the cub-octahedral sites and Sn atoms are octahedrally coordinated by I atoms. This characteristic perovskite (PVSK) lattice emphasizes the robust Sn–I framework that underpins both light absorption and charge transport. The charge density distribution shown in Fig. 1(b) reveals the strong localization of electronic density around iodine atoms, consistent with their high electronegativity. The pronounced intersection of Sn-5s and I-5p orbitals indicates mixed ionic-covalent bonding, which not only stabilizes the lattice but also enables defect tolerance, which is one of the defining attributes of halide PVSKs. Negligible charge accumulation at the Cs sites further confirms their role as electrostatic stabilizers rather than direct contributors to the frontier electronic states.

The electrostatic potential profile shown in Fig. 1(c) displays oscillations arising from the periodic arrangement of cations and anions. Deep potential wells appear at iodine sites, while shallower regions are associated with Cs atoms. The overall smooth variation of potential across the lattice reflects effective charge screening and reduced internal transport barriers. This stable electrostatic environment facilitates efficient charge separation and suppresses recombination when $CsSnI_3$ is integrated into device architectures. Overall, the charge density and electrostatic potential analyses underscore the electronic robustness of $CsSnI_3$. The mixed ionic-covalent bonding ensures structural stability, while the smooth electrostatic landscape promotes efficient carrier extraction, reinforcing its suitability as an efficient layer that absorbs light for lead-free PSCs.

In Fig. 2(a), the cubic PVSK lattice of $CsSnCl_3$ is shown, where Cs ions occupy the central A-site positions and Sn atoms are octahedrally coordinated by Cl atoms. Compared to $CsSnI_3$, the presence of smaller and more electronegative Cl ions leads to shorter Sn–Cl bonds, which significantly influence the material's electronic configuration and structural stability. The charge density distribution shown in Fig. 2(b) demonstrates strong localization around Cl atoms, reflecting their dominant role in bond formation. The overlap between Sn-5s and Cl-3p orbitals confirms mixed ionic-covalent bonding with a stronger ionic character than the Sn–I framework. This bonding nature reduces electronic polarizability, thereby widening the bandgap and enhancing the material's chemical robustness. As in $CsSnI_3$, the Cs atoms show negligible charge accumulation, serving mainly as electrostatic stabilizers.

The electrostatic potential profile shown in Fig. 2(c) reveals deeper potential wells at the Cl sites compared to the I sites in $CsSnI_3$, consistent with their higher electronegativity. The smooth potential distribution across the lattice indicates minimal internal barriers for charge transport, and the well-defined potential landscape contributes to defect tolerance by mitigating charge trapping and recombination at lattice imperfections. Overall, $CsSnCl_3$ exhibits a wide-bandgap electronic structure characterized by strong ionic bonding and stable electrostatic potential distribution. While this makes it less suitable as a primary light absorber, it is highly effective as a passivating and stabilizing capping layer in bilayer PSCs, complementing the visible-NIR absorption of $CsSnI_3$ and suppressing interfacial recombination.

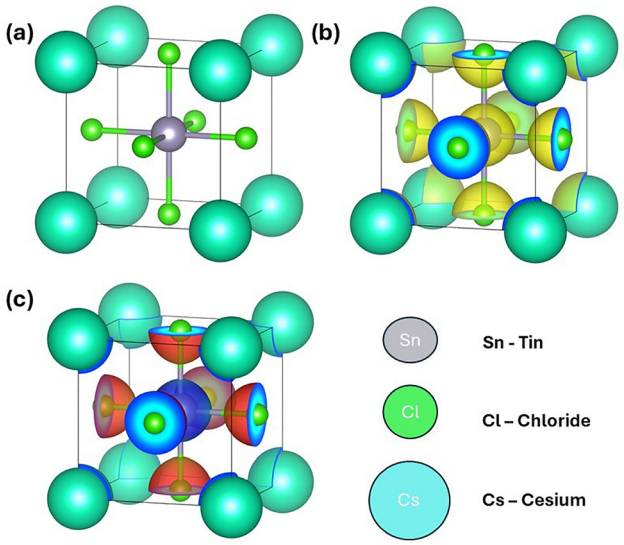

Fig. 2 (a) Crystal structure of the $CsSnCl_3$ perovskite, with Cs at the cub-octahedral site and Sn octahedrally coordinated by Cl atoms. (b) Charge density distribution showing strong localization around Cl atoms and partial hybridization of the Sn-5s and Cl-3p orbitals, reflecting a stronger ionic bonding character compared to $CsSnI_3$. (c) Electrostatic potential profile displaying deeper potential wells near the Cl sites and a stable potential landscape indicative of improved defect tolerance and enhanced chemical stability.

The charge density and electrostatic potential analyses of $CsSnI_3$ and $CsSnCl_3$ underscore their complementary roles in photovoltaic applications. $CsSnI_3$, characterized by strong Sn–I orbital hybridization and a relatively smooth electrostatic potential profile, exhibits efficient charge transport and broad absorption across the visible-NIR region. Thus, it is an excellent primary light-harvesting layer. Nevertheless, the comparatively weaker Sn–I bonding and limited chemical stability of $CsSnI_3$ lead to rapid degradation under ambient conditions. In contrast, $CsSnCl_3$ exhibits stronger ionic bonding and deeper electrostatic potential wells associated with Cl atoms, which impart a wider bandgap and significantly improved structural stability. Although its visible-light absorption is intrinsically limited, the stable potential landscape and defect-tolerant nature of $CsSnCl_3$ render it highly effective for suppressing interfacial recombination and passivating the $CsSnI_3$ surface. At the atomic level, the $CsSnCl_3$ capping layer provides field-effect passivation. Its wider bandgap and specific conduction band alignment create a potential barrier that prevents holes from reaching the electron-selective interface, thereby significantly reducing surface recombination velocities. Furthermore, the chloride-rich environment at the heterojunction can passivate iodine vacancies (V_I) in the $CsSnI_3$ layer a common trap state by forming stronger ionic Sn–Cl bonds that reduce the density of dangling bonds and suppress trap-mediated recombination.

Accordingly, in a bilayer configuration, $CsSnCl_3$ functions as a protective and electronically complementary layer that enhances open-circuit voltage and device stability, while $CsSnI_3$ remains the primary absorber responsible for photocurrent generation. This synergistic interplay between the narrow-bandgap, high-efficiency absorber ($CsSnI_3$) and the wide-bandgap, stabilizing partner ($CsSnCl_3$) provides a suitable foundation for the superior performance of the bilayer device compared with either constituent material alone.

3.2. Band structures of $CsSnI_3$ and $CsSnCl_3$

Fig. 3(a) presents the computed electronic band structure of $CsSnI_3$ across the high-symmetry directions (Γ–X–M–Γ–R–X|M–R) in the material's Brillouin zone. At 0 eV, the Fermi level is set and shown with a dashed horizontal line. The band dispersion reveals the semiconducting nature of $CsSnI_3$. The valence band maximum (VBM) and the conduction band minimum (CBM) are situated at the identical point, specifically the Γ point in reciprocal space, confirming a straight bandgap of around 1.2–1.3 eV. This bandgap value is consistent with those in previous reports for halide PVSKs and falls within the optimal range for photovoltaic applications. The conduction band displays significant curvature (dispersion), which suggests that the electrons have a small effective mass and, consequently, exhibit high mobility. Conversely, the relatively flat shape of the valence band implies that the holes are characterized by a heavier effective mass. Such electron–hole asymmetry is a hallmark of $CsSnI_3$-based PVSKs and plays an essential part in defining their charge movement characteristics.

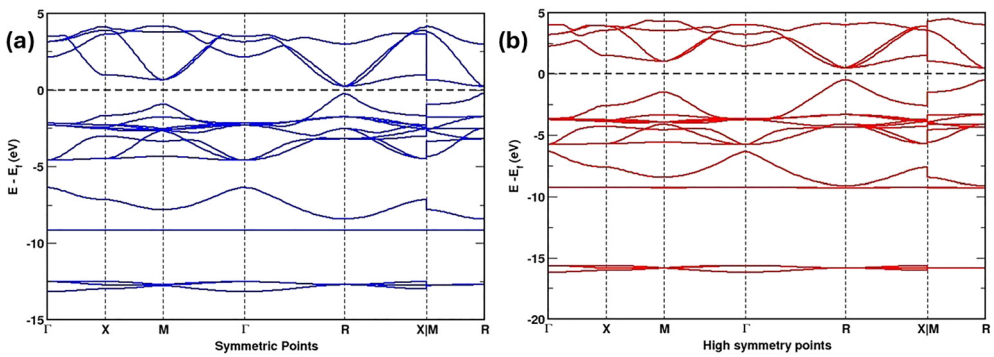

Fig. 3 Calculated electronic band structures of (a) $CsSnI_3$ and (b) $CsSnCl_3$ along high-symmetry paths of the material's Brillouin zone.

The orbital-resolved contributions further clarify the bonding and electronic structure. The deeper bands, located near 10 eV, arise primarily from iodine 5s states, while the valence band edge is dominated by hybridization among the I 5p and Sn 5s orbitals. Conversely, the states of the conduction band primarily originate from Sn 5p orbitals. This strong orbital interaction imparts covalent bonding characteristics and accounts for the significant band dispersion near the Fermi level. Overall, the results confirm that $CsSnI_3$ is a semiconductor that has a straight bandgap, effective band dispersion and favourable optoelectronic properties, reinforcing its potential as a highly promising lead-free absorber for PSC and related optoelectronic applications.

Fig. 3(b) illustrates the calculated electronic band structure of $CsSnCl_3$ along the high-symmetry directions (Γ–X–M–Γ–R–X|M–R) of the Brillouin zone, with the Fermi energy set to 0 eV (dashed line). The results reveal that $CsSnCl_3$ is a straight bandgap semiconductor that has a calculated bandgap of 2.2–2.4 eV within the GGA-PBE framework, slightly smaller than the experimentally reported value (~3.0 eV). The VBM and CBM are situated at the identical location, specifically the Γ point in reciprocal space, which verifies the direct bandgap nature of $CsSnCl_3$. The CBM, primarily composed of Sn-5p states, shows noticeable dispersion, indicative of light electron effective masses and efficient electron transport. By contrast, the valence band, largely dominated by Cl-3p states, is more localized, leading to heavier hole effective masses than those observed in $CsSnI_3$. The asymmetry is consistent with other wide-bandgap halide PVSK.

The deeper electronic states, spanning from approximately 10 eV to 15 eV, originate from strongly bound Sn–Cl orbitals that remain well separated from the frontier bands and contribute minimally to optical transitions. The flat nature of these deeper states underscores the stronger ionic bonding character of Sn–Cl compared to Sn–I. Collectively, these features highlight $CsSnCl_3$ as a chemically stable wide-bandgap PVSK with favourable electron transport properties and intrinsic transparency in the visible range. Owing to such attributes, it is a suitable wide-bandgap partner in bilayer device configurations, where it effectively passivates and stabilizes $CsSnI_3$ while complementing the strong visible NIR absorption of $CsSnI_3$.

3.3. Electronic band structure analysis of $CsSnI_3$ and $CsSnCl_3$ *via* partial density of states (PDOS)

The electronic structure of the $CsSnI_3$ and $CsSnCl_3$ perovskites was investigated using the PDOS, with the results presented in Fig. 4. For the $CsSnI_3$ layer (Fig. 4(a)), the VBM is predominantly formed by I 5p-orbital and Sn 5p-orbital hybridization, with a minor contribution from the Sn 5s-orbital. The CBM, on the other hand, is primarily composed of the Sn 5s-orbital, contributing significantly to the low electron effective mass and the favourable charge transport properties of $CsSnI_3$. The Cs 5s- and 5p-orbitals are located deeper within the valence band, confirming their inert role in the VBM and CBM formation.

In the $CsSnCl_3$ material (Fig. 4(b)), a similar contribution pattern is observed but with clear differences reflecting the wider bandgap introduced by the lighter halide element, Cl. The VBM is mainly derived from the hybridization of the Sn 5p-

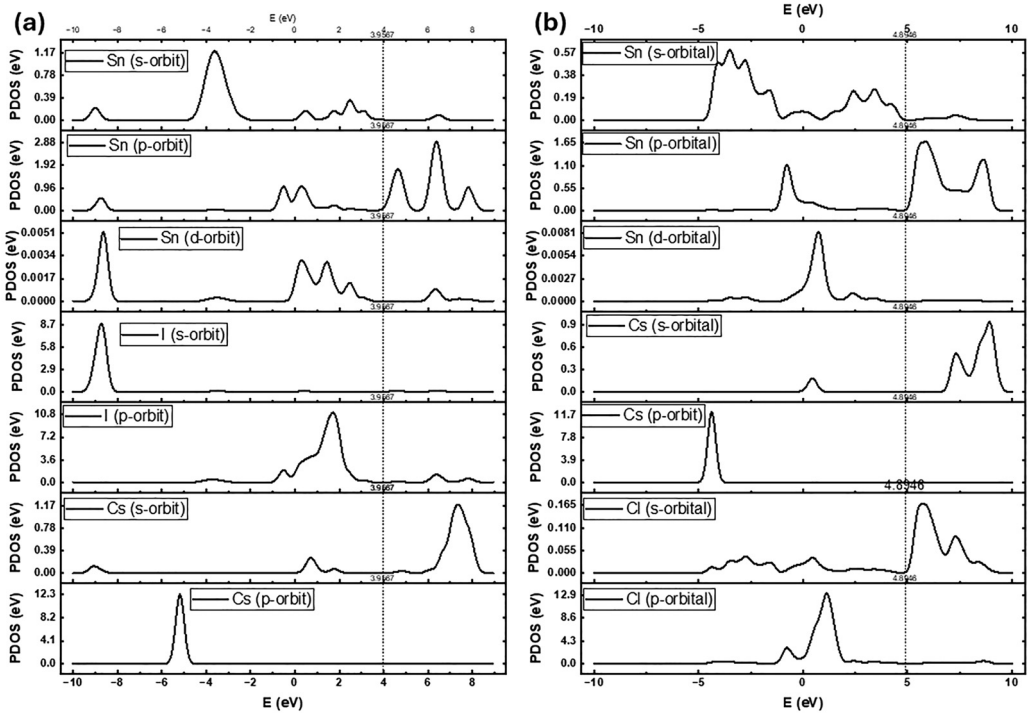

Fig. 4 Partial density of states (PDOS) for (a) $CsSnI_3$ and (b) $CsSnCl_3$, highlighting the orbital contributions to the VBM and CBM. The dashed vertical line indicates the Fermi level.

orbital and Cl 3p-orbital, again with some involvement from the Sn 5s-orbital. The CBM is still primarily dominated by the Sn 5s-orbital. The primary difference lies in the energy distribution: the VBM and CBM states are shifted to lower and higher energy values, respectively, relative to $CsSnI_3$. This shift leads to a larger bandgap for $CsSnCl_3$, which is essential for its function as a hole-blocking layer in the bilayer device. The substantial contribution of the Sn 5s and 5p states to the band edges in both compounds underscores the importance of the Sn cation oxidation state and coordination geometry in determining the overall electronic properties of these lead-free tin-based perovskites.

3.4. Energy band alignment of single and bilayer $CsSnI_3$/$CsSnCl_3$ absorbers

Fig. 5(a)–(c) illustrates the device architecture, where PCBM serves as the electron ETL; $CsSnI_3$, $CsSnCl_3$, or their bilayer acts as the PVSK absorbers; and CFTS functions as the HTL, using gold as the reverse connection and FTO as the fore contact. The corresponding energy band diagram (Fig. 5d) shows well-aligned conduction levels of $CsSnI_3$ (−3.6 eV) and $CsSnCl_3$ (−3.9 eV) with the CBM of PCBM (−3.9 eV), facilitating efficient electron extraction toward FTO. The valence bands of the absorbers (−4.9 eV for $CsSnI_3$ and −5.42 eV for $CsSnCl_3$) align favourably with CFTS (−4.6 eV), enabling effective hole transport to the Au electrode. Importantly, the bilayer configuration introduces a graded band alignment that couples the strong light absorption of $CsSnI_3$ with the enhanced stability and higher open-circuit voltage (V_{oc}) potential of $CsSnCl_3$, thereby suppressing recombination and improving charge separation.

Fig. 6 depicts the impact of band alignment on device performance for single and bilayer absorbers. In the $CsSnI_3$-based device (Fig. 6a), the positioning of the valence band peak of $CsSnI_3$ with the highest occupied state of CFTS enables effective hole extraction, although the relatively small conduction band offset at the $CsSnI_3$/PCBM interface may promote back-electron recombination and reduce charge selectivity. In contrast, the $CsSnCl_3$ device (Fig. 6b) benefits from a wider bandgap and higher CBM, which enhance electron blocking on the HTL side. However, the larger mismatch with CFTS impedes hole transport, accounting for its poor efficiency when paired with CFTS. The bilayer configuration (Fig. 6c) effectively integrates the advantages of both absorbers: $CsSnI_3$ contributes strong visible-light absorption, while the $CsSnCl_3$ capping layer improves alignment at the ETL interface, suppresses electron backflow, and enables graded band alignment. This synergistic arrangement promotes smoother carrier transport, reduces interfacial recombination, and highlights bilayer heterostructures as a promising route toward high-performance, lead-free PSCs.

3.4.1. Performance of $CsSnI_3$ single-junction PSC. The optimization of the $CsSnI_3$ absorber layer thickness is essential for optimizing single-junction PSC performance, as demonstrated by the systematic improvement in all the photovoltaic parameters when increasing the thickness from 0.1 to 1.5 μm (Table S1). Across this range, the J_{sc} exhibited the most significant enhancement, soaring from 11.95 mA cm^{-2} to 30.73 mA cm^{-2}. This substantial increase in current is primarily attributed to the extended optical path allowing for more efficient light absorption and corresponding photocarrier generation (Fig. 7a). Concurrently, the V_{oc} showed a modest but favourable rise, expanding from 0.97 V to a peak of 1.03 V, a signal at the interfaces of decreased non-radiative recombination. The FF remained consistently high and stable, increasing slightly from 87.01% to 88.22% (Fig. 7b), which confirms a robust and low-resistance charge transport even with the

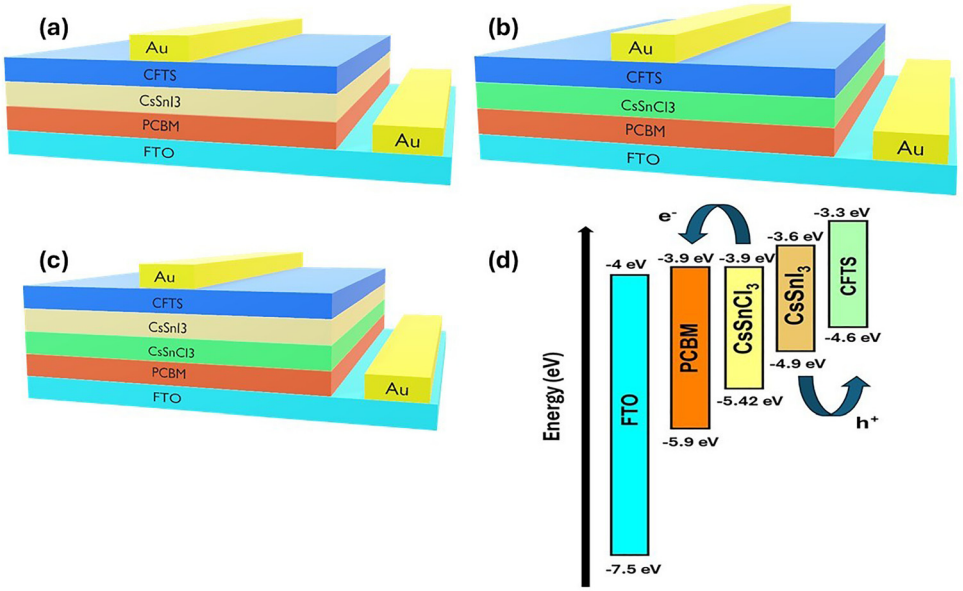

Fig. 5 Schematic of the proposed device structures and their corresponding band alignment. (a) FTO/PCBM/$CsSnI_3$/CFTS/Au, (b) FTO/PCBM/$CsSnCl_3$/CFTS/Au, and (c) FTO/PCBM/$CsSnCl_3$/$CsSnI_3$/CFTS/Au. (d) Energy level diagram illustrating the alignment of CBM and VBM of each layer.

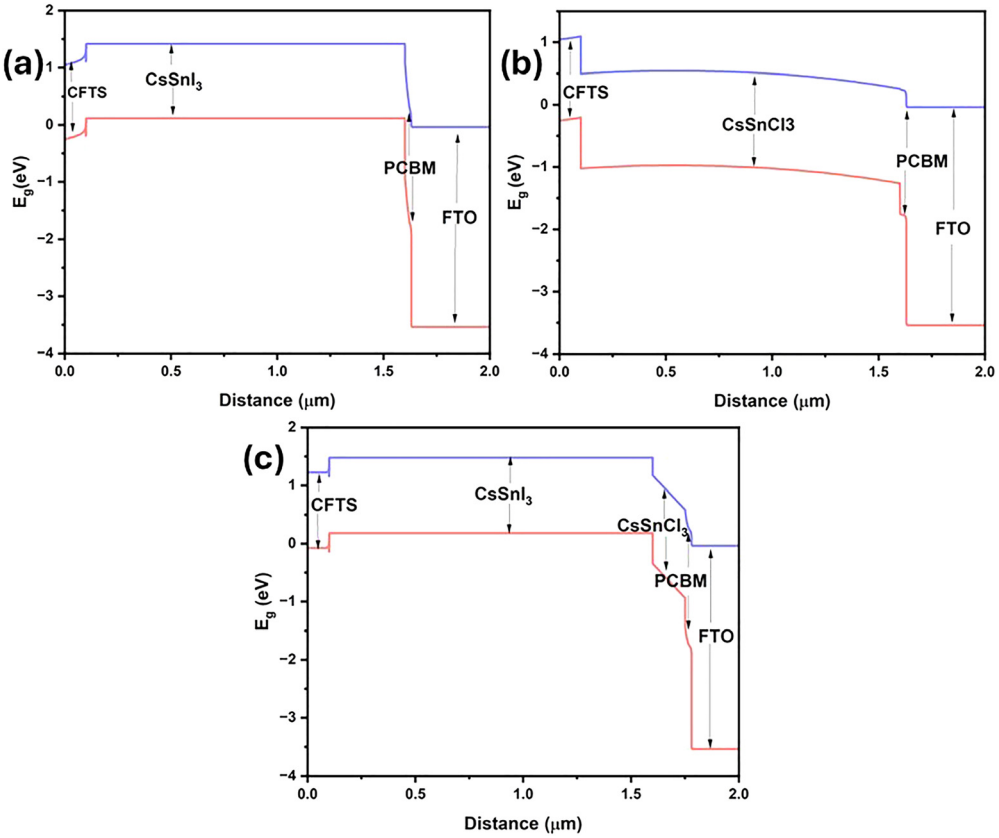

Fig. 6 Simulated energy band diagrams for (a) $CsSnI_3$, (b) $CsSnCl_3$, and (c) the bilayer $CsSnI_3$/$CsSnCl_3$ PVSK absorber integrated with CFTS and PCBM.

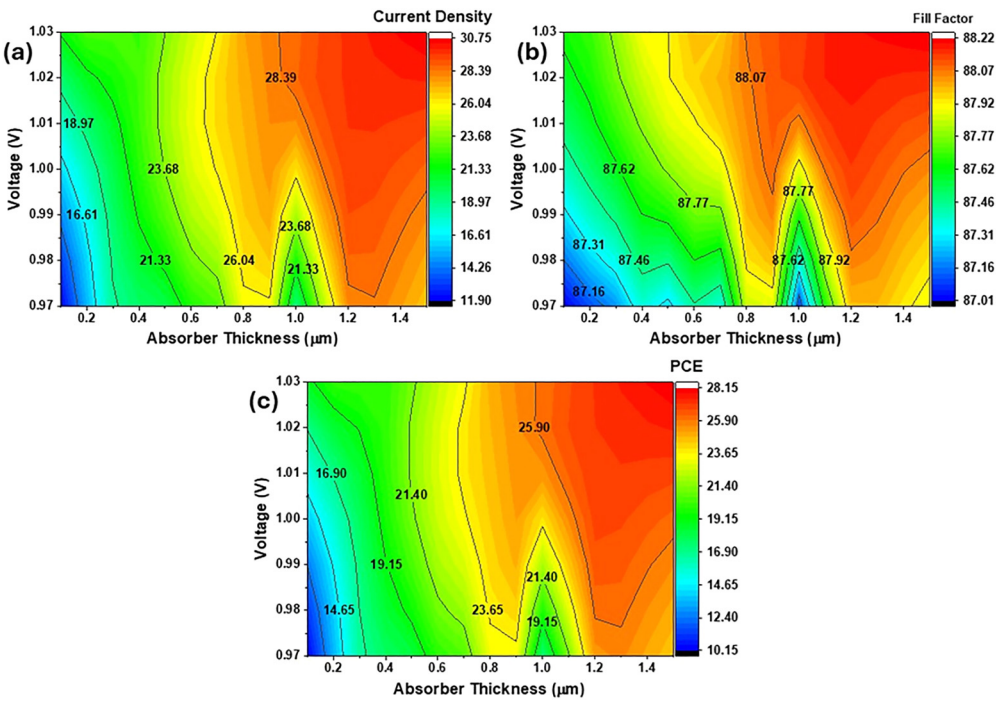

Fig. 7 Contour diagrams illustrating the effect of the $CsSnI_3$ absorber thickness (0.1–1.5 μm) and operating voltage (*V*) on the key photovoltaic parameters of the single-junction PSCs: (a) J_{sc}, (b) FF, and (c) PCE. These diagrams demonstrate a systematic enhancement across all parameters with increasing thickness, achieving an optimal performance (PCE = 28.12%) at 1.5 μm (data presented in Table S1).

thickening layer. The collective effect of these parameter enhancements resulted in a dramatic increase in the PCE, escalating from 10.16% to its maximum value of 28.12% at 1.5 μm (Fig. 7c). This confirms that a thickness of 1.5 μm provides the optimal balance, successfully boosting the photocurrent without introducing significant bulk recombination or transport limitations that would otherwise compromise performance.

3.4.2. Performance of $CsSnCl_3$ single-junction PSC. The solar efficiency of the $CsSnCl_3$ PSC was rigorously investigated by changing the absorber layer thickness, revealing an optimal operating point resulting from a critical balance in the carrier collection and photon absorption. As shown in Fig. 8(a), the J_{sc} sharply increases from 19.43 mA cm^{-2} to 28.22 mA cm^{-2} as the thickness is increased from 0.1 μm to 0.9 μm (detailed values are provided in Table S2), driven by enhanced light harvesting. Simultaneously, the FF exhibits an inverse relationship, decreasing from a peak of 75.65% at 0.2 μm to 73.83% at 0.9 μm (Fig. 8(b)), which is attributed to a higher resistance in series and bulk recombination losses in the thicker films. Thus, the PCE (Fig. 8(c)), which is the product of these factors, reaches its maximum of 15.75% within the narrow optimal window of 0.9 μm to 1.0 μm, demonstrating that this thickness range provides the best compromise between high photogeneration (high J_{sc}) and efficient charge extraction (sufficient FF). This validates the potential of $CsSnCl_3$ as a high-performing, lead-free absorber material.

3.4.3. Performance of bilayer $CsSnI_3$/$CsSnCl_3$ PSC. The photovoltaic performance of the $CsSnI_3$/$CsSnCl_3$ bilayer solar cell exhibits exceptional characteristics, peaking at the largest simulated thickness, which suggests that the optimal thickness is likely greater than 1.5 μm. Fig. 9(a) illustrates how the J_{sc} rises steadily and dramatically from 20.81 mA cm^{-2} at 0.1 μm to a high value of 32.09 mA cm^{-2} at 1.5 μm (Table S3), confirming maximized photon absorption by the narrow-bandgap $CsSnI_3$ layer. Importantly, the FF remains consistently high and stable across all thicknesses (Fig. 9(b)), increasing slightly from 87.85% to 88.54% over the same range, indicating that the wide-bandgap $CsSnCl_3$ layer effectively minimizes interfacial and bulk recombination losses, preserving the high collection efficiency even in the thickest film. This synergistic effect leads to a PCE (Fig. 9(c)) that rises monotonically, achieving a high value of 30.02% at 1.5 μm (with a peak over 31% in the contour map). This validates the $CsSnI_3$/$CsSnCl_3$ bilayer as a highly effective architecture for achieving high-performance, lead-free tin-based PSCs.

3.5. Impact of interface defect density on $CsSnI_3$/$CsSnCl_3$ solar cell performance

The electrical characteristics of the $CsSnI_3$/$CsSnCl_3$ PSC, including the PCE, FF, V_{oc}, and J_{sc}, exhibit a strong dependency on the interface defect density, as shown in Fig. 10. A minimal impact is observed in the low defect density regime (1×10^{10} to 1×10^{14} cm^{-2}), where V_{oc} (approx. 1.05 V), J_{sc} (approx. 32.07 mA cm^{-2}), and FF (approx. 86.5%) remain stable, resulting in a high PCE (29.16% to 26.54%). However, as the defect density increases beyond 1×10^{14} cm^{-2}, a sharp degradation occurs across all performance metrics. Crucially, the V_{oc} experiences a significant drop (Fig. 10(a)), falling sharply from 1.01 V at 1×10^{13} cm^{-2} to 0.84 V at 1×10^{16} cm^{-2} and saturating at 0.80 V above 1×10^{18} cm^{-2}.

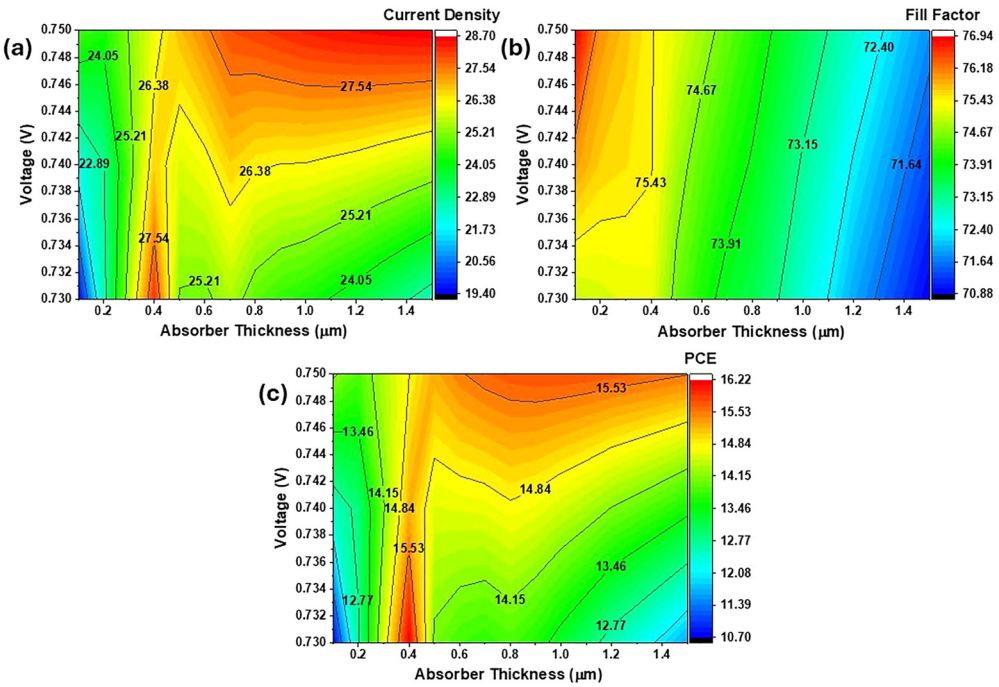

Fig. 8 Contour maps show the $CsSnCl_3$ PSC's simulated performance characteristics in relation to the voltage and thickness of the $CsSnCl_3$ absorber: (a) J_{sc}, (b) FF, and (c) PCE, with an optimized performance (PCE ~ 15%) achieved at 1.5 μm (Table S2).

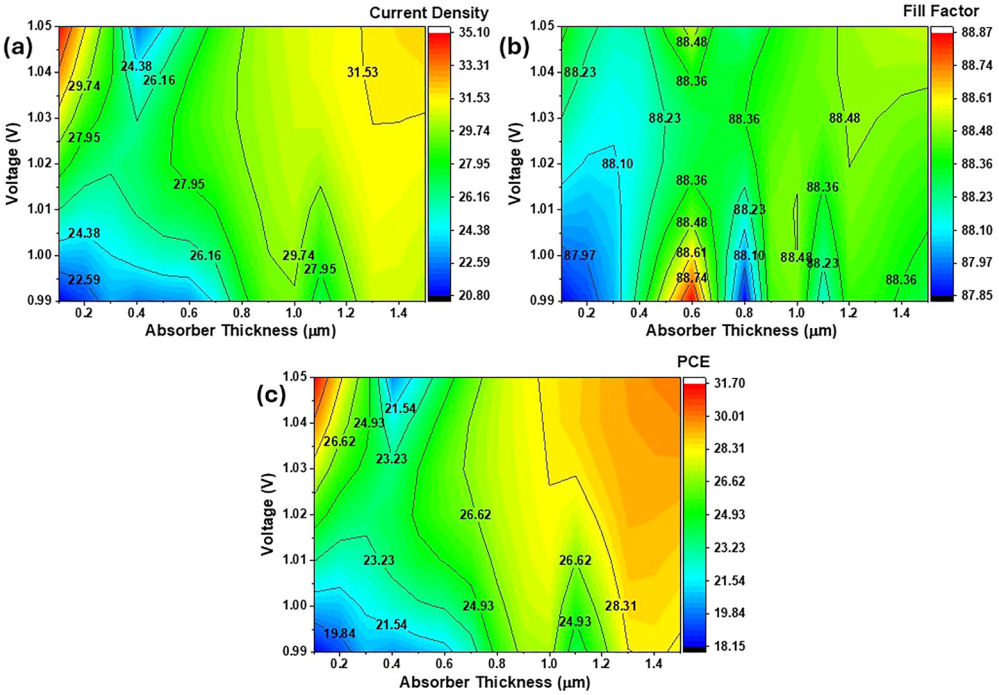

Fig. 9 Contour maps of the simulated performance parameters of the bilayer $CsSnI_3/CsSnCl_3$ PSC cell as a function of the total absorber thickness and voltage: (a) J_{sc}, (b) FF, and (c) PCE, with optimized performance (~30%) achieved at 1.5 μm (Table S3).

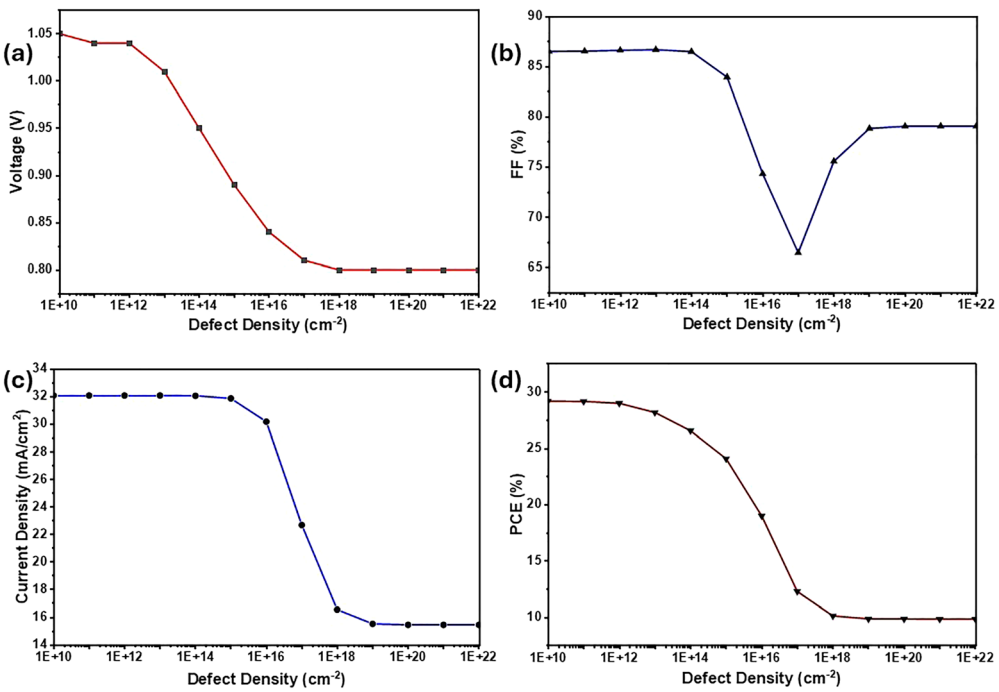

Fig. 10 Dependence of the $CsSnI_3/CsSnCl_3$ solar cell performance parameters (a) V_{oc}, (b) FF, (c) J_{sc}, and (d) PCE on the interface defect density, illustrating a critical degradation threshold above 1×10^{14} cm^{-3}.

Similarly, the J_{sc} (Fig. 10(c)) remains high until 1×10^{15} cm^{-2} (31.86 mA cm^{-2}) and then sharply plummets to 15.45 mA cm^{-2} at 1×10^{20} cm^{-2}. This severe reduction in the V_{oc} and J_{sc} confirms that these interface defects act as efficient recombination centers, severely limiting carrier extraction and collection. This synergistic degradation leads to a monotonic fall in the PCE (Fig. 10(d)), which experiences its steepest decline between 1×10^{16} cm^{-2} and 1×10^{18} cm^{-2} (dropping from 18.99% to 10.14%) and eventually stabilizes at approximately 9.86% for defect densities exceeding 1×10^{20} cm^{-3}, demonstrating the

critical need for defect passivation in the $CsSnI_3/CsSnCl_3$ device architecture.

3.6. Impact of bulk defect density in the $CsSnCl_3$ layer on bilayer solar cell performance

The photovoltaic performance of the $CsSnI_3/CsSnCl_3$ bilayer solar cell, with a fixed low defect density in the $CsSnI_3$ layer (1×10^{13} cm^{-3}), is critically dependent on the bulk defect density within the $CsSnCl_3$ layer, as shown in Fig. 11. At low $CsSnCl_3$ bulk defect densities (1×10^{10} to 1×10^{15} cm^{-3}), the device exhibits outstanding stability and high performance: the V_{oc} remains stable at approximately 1.05 V (Fig. 11(a)), the J_{sc} maintains its maximum value of approx. 32.09 mA cm^{-2} (Fig. 11(c)), and the FF remains high at approx. 88% (Fig. 11(b)).

This robust performance translates to a peak PCE of 30.03% (Fig. 11(d)). However, the performance undergoes a severe collapse as the $CsSnCl_3$ defect density increases beyond 1×10^{15} cm^{-3}. It should be noted that the degradation in the V_{oc} and FF is the primary driver of this failure. The V_{oc} starts to drop at 1×10^{16} cm^{-3} (1.02 V) and falls sharply to 0.40 V at 1×10^{20} cm^{-3}. Simultaneously, the FF plunges dramatically from 86.51% at 1×10^{15} cm^{-3} to only 21.54% at 1×10^{20} cm^{-3}, indicating a significant increase in bulk recombination losses and internal resistance within the electron transport layer. This leads to a catastrophic reduction in the PCE, which plummets from 25.43% at 1×10^{16} cm^{-3} to a marginal 0.23% at 1×10^{20} cm^{-3}, demonstrating the extreme sensitivity of the overall device efficiency to the crystalline quality of the wide-bandgap $CsSnCl_3$ layer.

3.7. Photovoltaic characteristics and thickness-dependent studies

The comparative analysis clearly establishes the superiority of the $CsSnI_3/CsSnCl_3$ bilayer architecture over its single-layer counterparts, achieving the highest PCE of 30.02% (Fig. 12(c)). This performance significantly surpasses those of the single-layer $CsSnI_3$ and $CsSnCl_3$ cells of 28.12% and 14.12%, respectively. The $CsSnI_3$ layer provides the necessary narrow bandgap for strong light absorption, resulting in a high V_{oc} of 1.05 V and a high J_{sc} of 32.09 mA cm^{-2}, substantially better than those of the $CsSnCl_3$ cell of 0.74 V and 24.89 mA cm^{-2}, respectively (Fig. 12(a) and (b)). Importantly, the introduction of the $CsSnCl_3$ layer into the bilayer structure enhances the performance metrics beyond those of the pure $CsSnI_3$ cell, boosting the J_{sc} from 30.73 to 32.09 mA cm^{-2} and maintaining an exceptional FF of 88.54%.

The analysis of the PCE curves shown in Fig. 12(d) strongly supports the $CsSnI_3/CsSnCl_3$ bilayer as the optimal structure, particularly in its ability to maintain a superior PCE across all tested thicknesses. When the thickness of absorber is 0.1 μm, the bilayer structure already exhibits a superior PCE of 18.19%, which is significantly higher than those of the $CsSnI_3$ and $CsSnCl_3$ cells at 10.16% and 10.71%, respectively. The single-layer $CsSnCl_3$ cell rapidly reaches its maximum PCE of 15.75% around 0.9 μm, and this PCE begins to decrease to 15.54% at 1.5 μm, demonstrating clear saturation and performance degradation in thicker films. In stark contrast, the bilayer and $CsSnI_3$ cells continue their growth: at 1.5 μm, the $CsSnI_3$ cell reaches 28.12%, while the bilayer maintains its lead, achieving the overall maximum efficiency of 30.02%. The fact that the bilayer

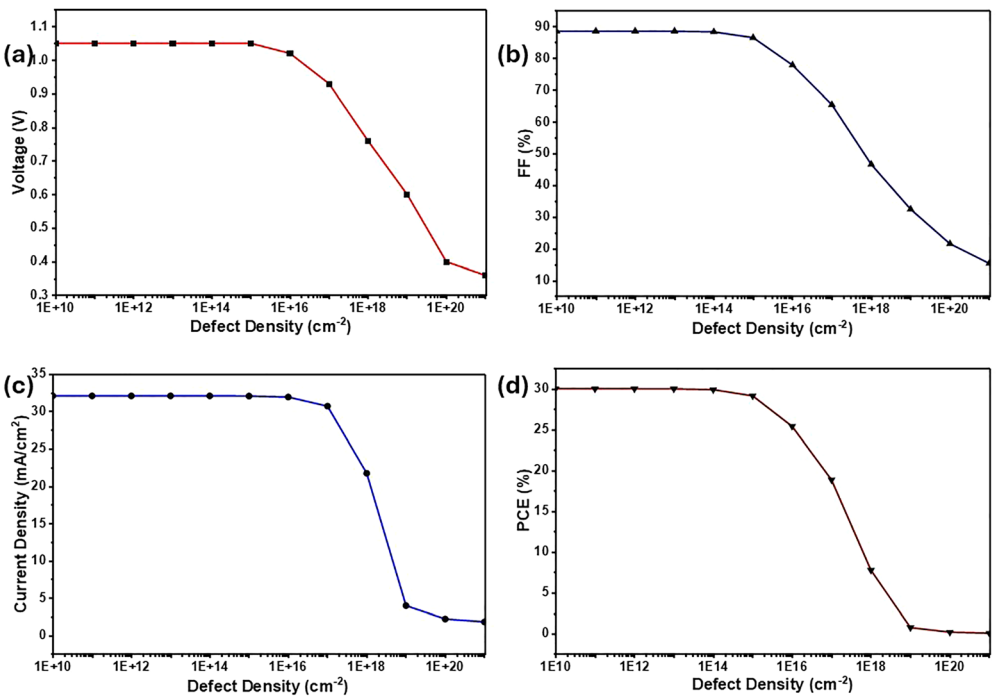

Fig. 11 Dependence of the $CsSnI_3/CsSnCl_3$ bilayer solar cell performance parameters (a) V_{oc}, (b) FF, (c) J_{sc}, and (d) PCE on the bulk defect density of the $CsSnCl_3$ layer, illustrating a critical degradation threshold above 1×10^{15} cm^{-3}.

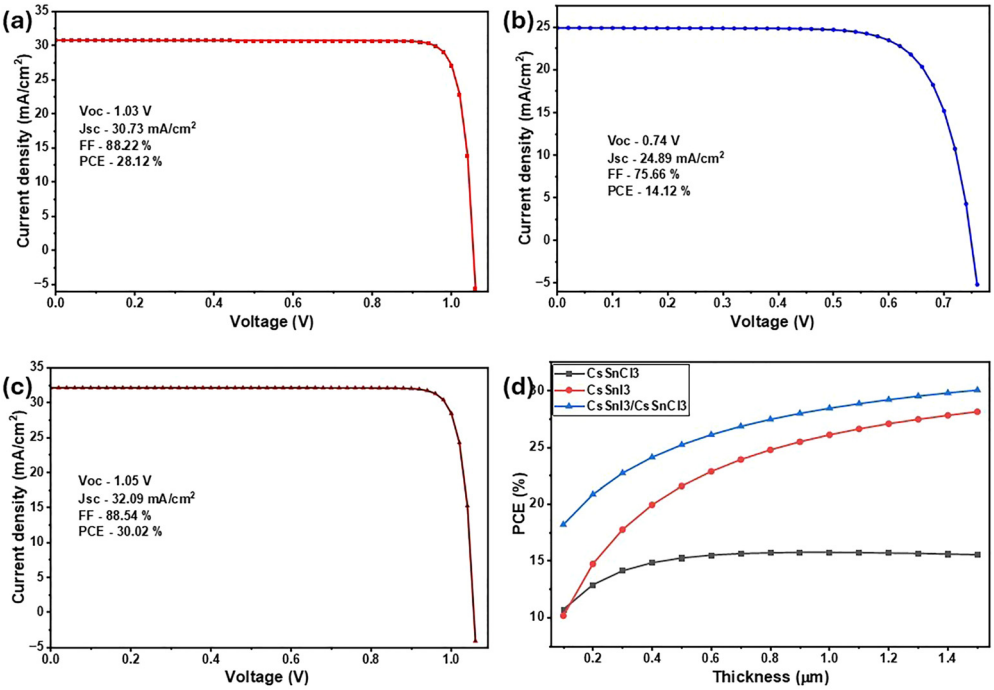

Fig. 12 *J*–*V* characteristics or current density–voltage for the (a) single-layer $CsSnI_3$ cell, (b) single-layer $CsSnCl_3$ cell, and (c) bilayer $CsSnI_3$/$CsSnCl_3$ cell measured at their respective optimal operating points. (d) PCE for each of the three variants shown against the thickness of the entire absorber layer.

PCE consistently increases up to the final measured thickness of 1.5 μm confirms its structural advantage in combining high photogeneration with efficient charge collection through minimized recombination. Thus, it is the highest performing and most promising configuration for further optimization beyond the simulated thickness range.

3.8. Analysis of quantum efficiency for single and bilayer PSCs

The wavelength-dependent external quantum efficiency (EQE) of $CsSnI_3$, $CsSnCl_3$, and their bilayer configuration is shown in Fig. 13, revealing distinct absorption behaviors for each device type. The $CsSnI_3$ single absorber exhibits a strong photo response beginning at ~310 nm, with the EQE rising to a maximum of ~95% around 360–380 nm and remaining above 90% until ~600 nm. Beyond this range, the EQE gradually decreases, falling below 80% near 800 nm and reaching ~74% at 900 nm, reflecting its narrow bandgap (~1.3 eV) that allows efficient visible-light absorption but limits response in the near-infrared. In contrast, the $CsSnCl_3$ single absorber shows a much weaker response across the spectrum, peaking at ~44% within the range of 300–330 nm and declining steadily to ~14% at 900 nm. This limited performance is consistent with its wide bandgap (~3 eV), which confines absorption primarily to the UV region.

The bilayer $CsSnI_3$/$CsSnCl_3$ device, however, effectively combines the strong visible-light absorption of $CsSnI_3$ with the UV response of $CsSnCl_3$, producing a broader and enhanced EQE spectrum. In this configuration, the EQE exceeds 98% in the 350–600 nm range, surpassing the performance of both individual absorbers, remaining above 90% even at longer wavelengths (~700–800 nm), where the $CsSnI_3$ absorber begins to decline, and the $CsSnCl_3$ absorber contributes minimally. These results demonstrate that the bilayer architecture leverages the complementary absorption properties of both materials, capturing UV photons *via* $CsSnCl_3$ and visible photons *via* $CsSnI_3$, which leads to superior photon-to-electron conversion. This synergistic effect accounts for the

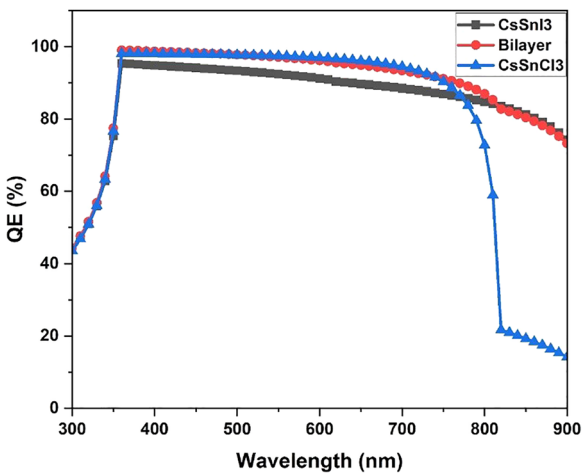

Fig. 13 Spectra of external quantum efficiency (EQE) for the $CsSnI_3$, $CsSnCl_3$, and bilayer $CsSnI_3$/$CsSnCl_3$ devices. $CsSnI_3$ provides strong absorption across the visible-NIR range, while $CsSnCl_3$ contributes in the UV region. The bilayer exhibits an enhanced and extended response, with EQE > 98% within the range of 350–600 nm and sustained >90% up to 800 nm.

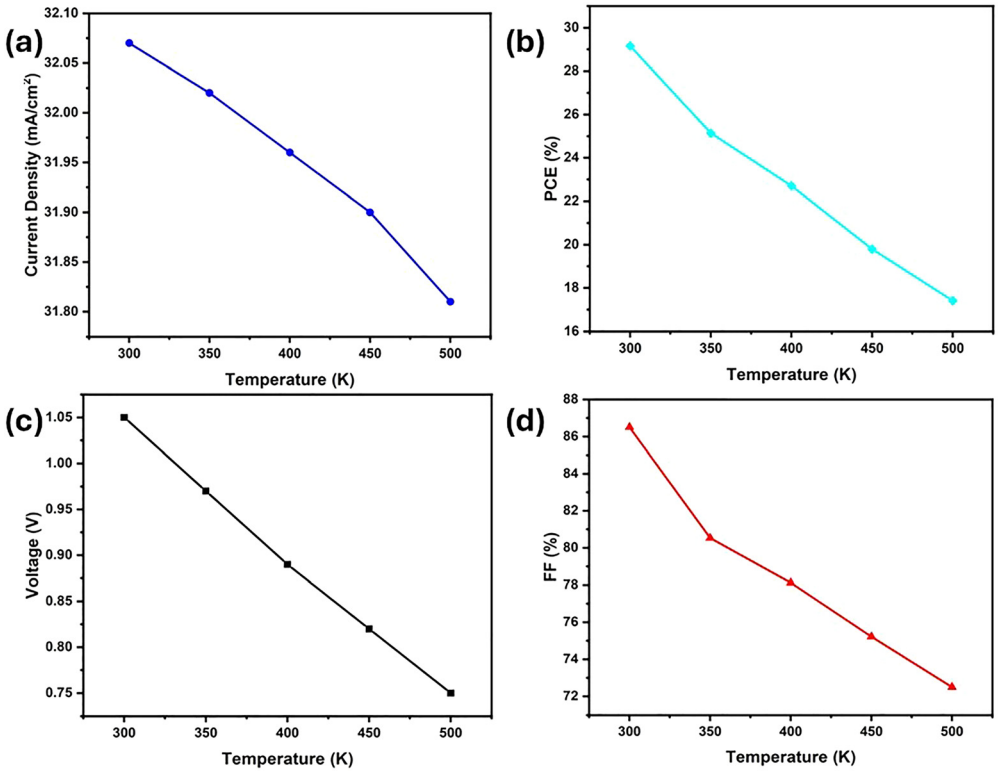

Fig. 14 Temperature-dependent photovoltaic parameters of the bilayer $CsSnI_3/CsSnCl_3$ solar cell from SCAPS-1D simulations: (a) J_{sc}, (b) PCE, (c) V_{oc}, and (d) FF in the range of 300–500 K. All the parameters show a monotonic decline with an increase in temperature, with the strongest effect observed for the V_{oc}.

higher J_{sc} and overall PCE observed in the bilayer solar cell compared to those of the single-absorber devices.

3.9. Temperature-dependent photovoltaic performance of bilayer $CsSnI_3/CsSnCl_3$ PSCs

The temperature-dependent performance of the bilayer $CsSnI_3/CsSnCl_3$ PSC was systematically evaluated within the range of 300–500 K using SCAPS-1D simulations. As shown in Fig. 14, all the photovoltaic parameters exhibit a monotonic degradation with an increase in temperature. The J_{sc} (Fig. 14a) shows only a marginal decline, suggesting that the photogeneration of carriers remains largely unaffected. In contrast, the V_{oc} (Fig. 14c) decreases sharply because of enhanced nonradiative recombination and a reduction in the built-in potential, while the FF (Fig. 14d) decreases progressively, reflecting increased series resistance and transport losses at elevated temperatures. Consequently, the PCE (Fig. 14b) undergoes a pronounced reduction of nearly 40% across the investigated range, primarily governed by the V_{oc} decline, followed by FF losses, with the J_{sc} contributing minimally. These results underscore the intrinsic thermal instability of the $CsSnI_3/CsSnCl_3$ bilayer architecture and highlight the importance of defect passivation and interface optimization to mitigate recombination pathways and ensure stable operation under practical device conditions.

3.10. Performance comparison of single and bilayer PSC based on SCAPS-1D simulations

The simulated PSC parameters presented in Table 3 emphasize the relative performance of $CsSnI_3$, $CsSnCl_3$, and their bilayer configuration alongside previously reported Sn- and Pb-based

Table 3 Simulated photovoltaic performance (PCE, FF, J_{sc}, and V_{oc}) of $CsSnI_3$, $CsSnCl_3$, and $CsSnI_3/CsSnCl_3$ bilayer PSCs alongside values reported in previous studies

Device architecture	V_{oc} (V)	J_{sc} (mA cm^{-2})	FF (%)	PCE (%)	Ref.
FTO/TiO_2/$CsPbI_3$/$FaPbI_3$/spiro/Au	1.10	24.50	74.00	19.94	33
ITO/TiO_2/$CsSnI_3$/$CsSnCl_3$/spiro-OMeTAD/Au	0.96	28.55	85.87	24	34
ITO/PCBM/$CsSnI_3$/CFTS/Se	0.87	33.99	83.46	24.73	27
ITO/PCBM/$CsSnI_3$/CuI/Au	0.91	14.24	78.11	10.11	35
FTO/PCBM/$CsSnCl_3$/PTAA/Au	1.3	15.34	89.90	17.93	36
ITO/TiO_2/$CsSnCl_3$/CBTS/Au	1.01	26.22	82.03	21.75	26
FTO/PCBM/$CsSnI_3$/CFTS/Au	1.03	30.73	88.22	28.12	This work
FTO/PCBM/$CsSnCl_3$/CFTS/Au	0.74	24.89	75.66	14.12	This work
FTO/PCBM/$CsSnCl_3$/$CsSnI_3$/CFTS/Au	1.05	32.09	88.54	30.02	This work

PSCs. Devices based on $CsSnI_3$ demonstrate strong photovoltaic characteristics, with the simulation yielding the following: PCE = 28.12%, FF = 88.22%, J_{sc} = 30.73 mA cm^{-2}, and V_{oc} = 1.03 V, which are competing with or superior to those of earlier $CsSnI_3$-based architectures. In contrast, $CsSnCl_3$ alone delivers a much weaker performance (FF = 75.66%, V_{oc} = 0.74 V, J_{sc} = 24.89 mA cm^{-2}), resulting in a low PCE of 14.12%, confirming its limited suitability as a primary absorber. Remarkably, the bilayer $CsSnI_3$/$CsSnCl_3$ device achieves the following: PCE = 30.02%, FF = 88.54%, J_{sc} = 32.09 mA cm^{-2}, and V_{oc} = 1.05 V, surpassing those of both single absorbers and most reported structures. These findings underscore the synergistic advantage of bilayer engineering, where $CsSnCl_3$ functions as an efficient passivation and stabilizing interfacial layer, thereby enhancing the V_{oc} and overall device efficiency well beyond the values achieved in previous studies.

While the simulated PCE of 30.02% represents a near-ideal theoretical limit, practical implementation presents several experimental hurdles. The main obstacle is the swift oxidation of Sn^{2+} into Sn^{4+} under ambient conditions,[39,40] resulting in significant p-type self-doping and deep-level traps that cause intense non-radiative recombination. Achieving the high performance predicted here would require stringent oxygen-free processing, advanced encapsulation, and the use of chemical additives to stabilize the Sn^{2+} oxidation state and maintain the low defect densities (10^{13} cm^{-3}) assumed in our optimal model.

4. Conclusion

In the final analysis, the $CsSnI_3$/$CsSnCl_3$ bilayer solar cell numerical investigation, conducted mainly through the SCAPS-1D simulation tool, confirms unambiguously its very high potential for serving as a lead-free and high-efficiency option. First, the initial DFT analysis confirmed the electronic properties, which facilitated the structural design, especially in confirming the beneficial Sn s- and p-orbital dominance at the band edges and the widening of the bandgap introduced by the $CsSnCl_3$ layer. The resulting graded bandgap design yielded a compelling peak PCE of 30.02% under optimal conditions. However, these simulations also provided critical insights that this performance is highly vulnerable to material defects: the PCE collapsed catastrophically when either the interface defect density surpassed 1×10^{14} cm^{-2} or the bulk defect density in each layer exceeded 1×10^{15} cm^{-3}. These losses were driven essentially by enhanced non-radiative recombination and subsequent V_{oc} and FF degradation. Thirdly, the thermal stability analysis showed that the device efficiency was negatively correlated to the increasing operating temperature, with V_{oc} loss as the major thermal degradation mechanism. Consequently, to ensure that the theoretical 30% efficiency of this promising $CsSnI_3$/$CsSnCl_3$ architecture is practicable, rigorous defect passivation techniques and effective thermal management methods are absolutely required.

Author contributions

Hariharan Rajasekaran contributed to writing, software, data curation, and formal analysis. Thangaraji Vasudevan handled writing, review, editing, and data curation. Lung-Chien Chen contributed to supervision, project administration, conceptualization, and funding. All authors approved the manuscript.

Conflicts of interest

The authors state that they have no financial conflicts of interest or personal relationships that could have affected the research presented in this paper.

Data availability

Supplementary information (SI) is available. See DOI: https://doi.org/10.1039/d5ma01437a.

Data cannot be shared openly but are available on request from the authors.

Acknowledgements

This research was supported by the Ministry of Science and Technology (MOST), Taiwan (Contract No. 111-2221-E-027-040-MY3), and the National Taipei University of Technology-Industry Joint Research Program, Taiwan (Contract No. 211A171).

References

1 X. Jiang, S. Qin, L. Meng, G. He, J. Zhang, Y. Wang, Y. Zhu, T. Zou, Y. Gong, Z. Chen, G. Sun, M. Liu, X. Li, F. Lang and Y. Li, *Nature*, 2024, **635**, 860–866.
2 J. Zhou, L. Tan, Y. Liu, H. Li, X. Liu, M. Li, S. Wang, Y. Zhang, C. Jiang, R. Hua, W. Tress, S. Meloni and C. Yi, *Joule*, 2024, **8**, 1691–1706.
3 Z. He, T. Luan, S. Zhang, Q. Wei, D. Huang, L. Wang, Y. Wang, P. Li and W. W. Yu, *Adv. Mater.*, 2024, **36**, 2410363.
4 F. Palazon, F. Di Stasio, Q. A. Akkerman, R. Krahne, M. Prato and L. Manna, *Chem. Mater.*, 2016, **28**, 2902–2906.
5 Y. Wang, J. Wan, J. Ding, J.-S. Hu and D. Wang, *Angew. Chem., Int. Ed.*, 2019, **58**, 9414–9418.
6 B. Saparov, J.-P. Sun, W. Meng, Z. Xiao, H.-S. Duan, O. Gunawan, D. Shin, I. G. Hill, Y. Yan and D. B. Mitzi, *Chem. Mater.*, 2016, **28**, 2315–2322.
7 S. J. Lee, S. S. Shin, Y. C. Kim, D. Kim, T. K. Ahn, J. H. Noh, J. Seo and S. I. Seok, *J. Am. Chem. Soc.*, 2016, **138**, 3974–3977.
8 F. Hao, C. C. Stoumpos, D. H. Cao, R. P. H. Chang and M. G. Kanatzidis, *Nat. Photonics*, 2014, **8**, 489–494.
9 H. Tsai, W. Nie, J.-C. Blancon, C. C. Stoumpos, R. Asadpour, B. Harutyunyan, A. J. Neukirch, R. Verduzco, J. J. Crochet, S. Tretiak, L. Pedesseau, J. Even, M. A. Alam, G. Gupta, J. Lou, P. M. Ajayan, M. J. Bedzyk, M. G. Kanatzidis and A. D. Mohite, *Nature*, 2016, **536**, 312–316.
10 N. K. Noel, S. D. Stranks, A. Abate, C. Wehrenfennig, S. Guarnera, A.-A. Haghighirad, A. Sadhanala, G. E. Eperon,

S. K. Pathak, M. B. Johnston, A. Petrozza, L. M. Herz and H. J. Snaith, *Energy Environ. Sci.*, 2014, **7**, 3061–3068.
11 Y. Shao, Y. Yuan and J. Huang, *Nat. Energy*, 2016, **1**, 15001.
12 W. Meng, B. Saparov, F. Hong, J. Wang, D. B. Mitzi and Y. Yan, *Chem. Mater.*, 2016, **28**, 821–829.
13 G. K. Gupta, A. Garg and A. Dixit, *J. Appl. Phys.*, 2018, **123**, 013101.
14 I. Chung, J.-H. Song, J. Im, J. Androulakis, C. D. Malliakas, H. Li, A. J. Freeman, J. T. Kenney and M. G. Kanatzidis, *J. Am. Chem. Soc.*, 2012, **134**, 8579–8587.
15 M. H. Kumar, S. Dharani, W. L. Leong, P. P. Boix, R. R. Prabhakar, T. Baikie, C. Shi, H. Ding, R. Ramesh, M. Asta, M. Graetzel, S. G. Mhaisalkar and N. Mathews, *Adv. Mater.*, 2014, **26**, 7122–7127.
16 K. Sun, J. Huang, J. Li, C. Yan and X. Hao, *Sci. China: Phys., Mech. Astron.*, 2022, **66**, 217302.
17 J. Shamsi, D. Kubicki, M. Anaya, Y. Liu, K. Ji, K. Frohna, C. P. Grey, R. H. Friend and S. D. Stranks, *ACS Energy Lett.*, 2020, **5**, 1900–1907.
18 M. Jeong, I. Choi, E. Go, Y. Cho, M. Kim, B. Lee, S. Jeong, Y. Jo, H. Choi, J. Lee, J.-H. Bae, S. K. Kwak, D. Kim and C. Yang, *Science*, 2020, **369**, 1615–1620.
19 B. Li, H. Di, B. Chang, R. Yin, L. Fu, Y. Zhang and L. Yin, *Adv. Funct. Mater.*, 2021, **31**, 2007447.
20 J. You, L. Meng, T.-B. Song, T.-F. Guo, Y. (Michael) Yang, W.-H. Chang, Z. Hong, H. Chen, H. Zhou, Q. Chen, Y. Liu, N. De Marco and Y. Yang, *Nat. Nanotechnol.*, 2016, **11**, 75–81.
21 D. Jeong, G.-U. Kim, D. Lee, S. Seo, S. Lee, D. Han, H. Park, B. Ma, S. Cho and B. J. Kim, *Adv. Energy Mater.*, 2022, **12**, 2201603.
22 R. Garai, R. K. Gupta, M. Hossain and P. K. Iyer, *J. Mater. Chem. A*, 2021, **9**, 26069–26076.
23 H. Song, X. Meng, Z. Wang, H. Liu and J. Ye, *Joule*, 2019, **3**, 1606–1636.
24 L. Wang, S. Yang, Q. Han, F. Yu, X. Cai, F. Liu, C. Zhang and T. Ma, *ACS Appl. Energy Mater.*, 2020, **3**, 9724–9731.
25 P. Gao, M. Grätzel and M. K. Nazeeruddin, *Energy Environ. Sci.*, 2014, **7**, 2448–2463.
26 M. K. Hossain, G. F. I. Toki, A. Kuddus, M. H. K. Rubel, M. M. Hossain, H. Bencherif, Md. F. Rahman, Md. R. Islam and M. Mushtaq, *Sci. Rep.*, 2023, **13**, 2521.
27 M. K. Hossain, M. S. Uddin, G. F. I. Toki, M. K. A. Mohammed, R. Pandey, J. Madan, Md. F. Rahman, Md. R. Islam, S. Bhattarai, H. Bencherif, D. P. Samajdar, M. Amami and D. K. Dwivedi, *RSC Adv.*, 2023, **13**, 23514–23537.
28 J. Balasubramaniyan, T. Vasudevan, G. Rajamanickam and L.-C. Chen, *Sol. Energy*, 2025, **302**, 113976.
29 G. F. I. Toki, M. K. Hossain, M. Shihab Uddin, A. M. Tawfeek, S. Rabhi, M. A. Darwish, R. Haldhar, D. K. Dwivedi, J. Madan and R. Pandey, *Inorg. Chem. Commun.*, 2024, **165**, 112439.
30 M. Burgelman, K. Decock, S. Khelifi and A. Abass, *Thin Solid Films*, 2013, **535**, 296–301.
31 P. Giannozzi, S. Baroni, N. Bonini, M. Calandra, R. Car, C. Cavazzoni, D. Ceresoli, G. L. Chiarotti, M. Cococcioni, I. Dabo, A. Dal Corso, S. de Gironcoli, S. Fabris, G. Fratesi, R. Gebauer, U. Gerstmann, C. Gougoussis, A. Kokalj, M. Lazzeri, L. Martin-Samos, N. Marzari, F. Mauri, R. Mazzarello, S. Paolini, A. Pasquarello, L. Paulatto, C. Sbraccia, S. Scandolo, G. Sclauzero, A. P. Seitsonen, A. Smogunov, P. Umari and R. M. Wentzcovitch, *J. Phys.: Condens. Matter*, 2009, **21**, 395502.
32 M. Burgelman, P. Nollet and S. Degrave, *Thin Solid Films*, 2000, **361–362**, 527–532.
33 A. Hajjiah, M. Gamal, I. Kandas, N. E. Gorji and N. Shehata, *Sol. Energy Mater. Sol. Cells*, 2022, **248**, 112026.
34 S. Baruah, J. Borah and S. Maity, *IEEE J. Quantum Electron.*, 2025, 1.
35 M. K. Hossain, G. F. I. Toki, D. P. Samajdar, M. Mushtaq, M. H. K. Rubel, R. Pandey, J. Madan, M. K. A. Mohammed, Md. R. Islam, Md. F. Rahman and H. Bencherif, *ACS Omega*, 2023, **8**, 22466–22485.
36 S. Srivastava, A. K. Singh, P. Kumar and B. Pradhan, *J. Appl. Phys.*, 2022, **131**, 175001.
37 O. Saidani, A. Yousfi, D. P. Samajdar, X. Xu, T. Biniyam Zemene, S. Bhattarai, M. K. Hossain and G. S. Sahoo, *Sol. Energy Mater. Sol. Cells*, 2024, **277**, 113122.
38 S. Sharma, M. Kumar, D. V. Singh, O. R. Herrera and J. M. Siqueiros, *Mater. Lett.*, 2024, **366**, 136472.
39 G. Venkateswarlu, C. V. M. Chaturvedi, U. Nanda, J. Bhaskara Rao, E. Sampad and N. Bodasingi, *Opt. Quantum Electron.*, 2025, **57**, 634.
40 G. Venkateswarlu, E. Sampad, U. Nanda, J. Bhaskara Rao, C. V. M. Chaturvedi and N. Bodasingi, *J. Electron. Mater.*, 2026, **55**, 873–890.